Materials Horizons

ROYAL SOCIETY OF CHEMISTRY

COMMUNICATION

View Article Online
View Journal

Cite this: DOI: 10.1039/d6mh00083e

Received 16th January 2026,
Accepted 27th March 2026

DOI: 10.1039/d6mh00083e

rsc.li/materials-horizons

Dual-target, high-capacity removal of microplastics and dyes from water using a recyclable sponge monolith

Ting Huang,†[a] Fangtian Liu,†[a] Yifei Liu,[a] Bingchen Wu,[a] Xiaowen Shi,[a] Yang Wu,*[a] Hongbing Deng *[a] and Xue Zhou*[b]

Microplastics, in combination with ubiquitous dye pollutants, pose a complex environmental challenge through synergistic interactions that enhance contaminant mobility and amplify ecological risks. To address this, we fabricate a monolithic, recyclable chitin/activated carbon sponge (CT/AC) *via* a scalable, crosslinker-free cryo-assembly method. This integrated sponge enables dual-target removal of microplastics and multiple dyes, overcoming the limitations of powdered adsorbents and flocculation processes by allowing direct retrieval without secondary release. The sponge exhibits exceptional co-removal performance, achieving record-high adsorption capacities of 1177.17 mg g^{-1} for 5 μm polystyrene (PS) microplastics, and 1038.86, 911.23, and 734.47 mg g^{-1} for rhodamine B, malachite green, and Congo red, respectively, even under challenging conditions (*e.g.*, high ionic strength, particulate interference, and humic acid). Life cycle assessment (LCA) confirms a low carbon footprint, attributable to renewable feedstocks and energy-efficient fabrication. Furthermore, the spent sponge is sustainably upcycled into graphene *via* flash Joule heating (FJH), enabling a closed-loop solution for advanced wastewater decontamination.

New concepts

This work proposes a new materials concept: an integrated, monolithic adsorption platform designed for holistic contaminant lifecycle management. It is realized through a scalable, crosslinker-free cryo-assembled chitin/activated carbon (CT/AC) sponge. This platform transcends conventional single-target, powdered adsorbents by enabling the simultaneous, high-capacity removal of both particulate (*e.g.*, microplastics, 1177 mg g^{-1}) and soluble (*e.g.*, multiple dye classes, 740–1039 mg g^{-1}) pollutants from complex aqueous matrices. Its key operational advance is the monolithic, directly retrievable architecture that eliminates secondary release and handling issues. The concept integrates three critical, differentiated advances: (1) exceptional co-removal efficacy under challenging conditions (high ionic strength and competing organics); (2) a robust macroscopic form enabling practical applications; and (3) a pre-designed sustainable lifecycle, from renewable feedstocks to end-of-life valorization of spent material into graphene *via* flash Joule heating, establishing a closed-loop pathway. This approach provides a fundamental materials science insight: true sustainability in environmental remediation requires a paradigm shift from optimizing discrete adsorption capacity to engineering multifunctional, structurally integrated systems where operational performance, scalable fabrication, and post-use resource recovery are co-designed from inception. It advances the field toward circular design principles in functional materials.

Introduction

The emerging threat of microplastic pollution intersects critically with the persistent issue of synthetic dyes in aquatic environments. Global dye production exceeds 1 million tons annually, with an estimated 80% of dye-containing wastewater, amounting to nearly 70 billion tons from the textile industry each year, being discharged untreated.[1] Concurrently, microplastics continue to accumulate in water systems, with approximately 150 million tons currently residing in aquatic environments and over 12 million tons entering the oceans annually.[2–6] When weathered, these microplastics undergo surface oxidation and fragmentation into micro/nanoplastics, developing enhanced adsorption capacities for organic pollutants.[7,8] Consequently, they not only accumulate but also effectively transport dyes over vast distances, compounding the environmental impact and necessitating the development of advanced treatment technologies capable of addressing both pollutants simultaneously.[9–11]

[a] *Hubei Key Laboratory of Biomass Resource Chemistry and Environmental Biotechnology, Hubei International Scientific and Technological Cooperation Base of Sustainable Resource and Energy, Hubei Engineering Center of Natural Polymers-based Medical Materials, School of Resource and Environmental Science, Wuhan University, Wuhan, 430079, China. E-mail: youngwuu@whu.edu.cn, hbdeng@whu.edu.cn*

[b] *Department of Occupational and Environmental Health, School of Public Health, Tongji Medical College, Huazhong University of Science and Technology, Wuhan, 430030, China. E-mail: xue.zhou@hust.edu.cn*

† These authors contributed equally to this work.

The co-occurrence of dyes and microplastics necessitates integrated remediation strategies. Although filtration has been demonstrated to be effective in capturing larger microplastic particles, it is largely ineffective against nanoplastics and dissolved dye molecules.[12,13] Conversely, adsorption provides a versatile and operationally simple platform for the simultaneous removal of both pollutant types. However, existing commercial adsorbents generally suffer from issues such as limited variety, low removal efficiency, and high production costs. Moreover, the utilization of powdered adsorbents has been shown to possess certain disadvantages in practical applications, including the challenges associated with their recovery and the potential for causing secondary pollution, which significantly restricts their effectiveness.[14,15] Consequently, there is an urgent need for the rational design of cost-effective, environmentally friendly, and highly efficient adsorbents to address this dual challenge in water treatment systems.

The development of high-performance adsorbents from widely available and low-cost biomass represents a promising strategy for sustainable water remediation. Chitin (CT), a natural structural polysaccharide abundantly derived from crustacean and fungal waste, has attracted significant interest due to its inherent eco-friendliness and unique cationic nature.[16] As the only naturally occurring cationic polysaccharide, CT possesses protonatable amino groups that confer a persistent positive surface charge, making it particularly effective for adsorbing negatively charged microplastics and dyes.[17–19] Concurrently, powdered activated carbon (AC) is widely recognized as a low-cost and highly effective adsorbent for a broad spectrum of dyes; however, its practical application is hampered by difficulties in recovery and the risk of secondary release.[20–23] Therefore, leveraging the innate nanofibrillar network of CT as a macroscopic scaffold presents a promising strategy to immobilize AC. Such an approach could effectively prevent AC leakage while synergistically combining the affinity of microplastic capture performance of CT with the dye adsorption capacity of AC, paving the way for efficient and recyclable adsorption platforms.[24]

Herein, we report a monolithic chitin/activated carbon sponge (CT/AC) for the dual-target, high-capacity removal of microplastics and dyes. The spent sponge can be further upcycled into graphene at the end of life. This monolith was fabricated using waste-derived CT and powdered AC, ensuring cost-effectiveness and scalability (Fig. 1A). Its structure is stabilized by electrostatic and hydrogen bonding interactions between CT and AC. Physical encapsulation by the CT nanofiber network further reinforces the architecture. This results in a robust three-dimensional macroporous adsorbent that fully immobilizes AC while preserving active sites. The CT/AC monolith achieves exceptional co-removal performance toward microplastics and multiple dyes. This performance may involve multiple interfacial mechanisms, including hydrophobic interaction, hydrogen bonding, π–π interaction, electrostatic interaction, pore filling, and physical interception (Fig. 1B). Furthermore, the spent sponge can be directly converted into graphene *via* FJH. This enables a closed-loop remediation strategy that highlights the practical potential of this dual-functional monolith for sustainable wastewater treatment.

Results and discussion

Construction of the self-assembled CT/AC monolithic sponge

The fabrication of the CT/AC composite sponge began with CT, and synergistic acid–mechanical treatment was employed to exfoliate the fibrous structure and expose the active groups, producing a homogeneous, amide-rich slurry.[25] AC powder was then introduced and uniformly mixed with CT *via* electrostatic interaction. Finally, freeze-drying and hydrogen bond-mediated self-assembly yielded a porous CT/AC network without the use of cross-linking agents (Fig. 2A).[17] Compared to the dispersed state of AC in water, the CT fibers bonded with AC *via* electrostatic interactions, forming a uniform and stable dispersion system without precipitation or stratification after standing (Fig. 2B). This slurry can be easily injected into various molds to prepare large-scale sponges (Fig. 2C), demonstrating potential for large-scale applications. Microscopic observation revealed that AC in water tended to agglomerate and settle, with the size exceeding 100 μm, whereas in the CT slurry, AC was uniformly dispersed with significantly reduced agglomeration, indicating the exceptional dispersion stability of CT for AC (Fig. 2D and E).[26,27]

X-ray microscopy (XRM) images showed the uniform low-density porous structure with CT fibers and AC particles (Fig. 2F). Scanning electron microscopy (SEM) results further revealed that the pure CT sponge possessed a regular lamellar structure, providing abundant active sites for AC loading (Fig. 2G). The AC powder, with various shapes and sizes (Fig. S1), was embedded within the fibrous network and attached to the lamellar surfaces. This indicated uniform dispersion and good integration between the CT and AC components during compounding (Fig. 2H).

Fourier transform infrared (FTIR) spectra (Fig. S2A) of both CT and CT/AC_5 exhibited characteristic peaks of CT at 3436 cm^{-1} (O–H stretch), 3280 cm^{-1} (N–H stretch), 1652 cm^{-1} and 1558 cm^{-1} (amide I and II bands), and 1378 cm^{-1} (C–H deformation vibration).[28] Raman spectroscopy revealed that the D and G bands of AC (1300 cm^{-1} and 1500 cm^{-1}, respectively) were preserved in CT/AC_5, with an intensity ratio (I_D/I_G) of about 1, indicating the maintenance of the sp^2 carbon structure of AC during compounding. The disappearance of the peak at 1100 cm^{-1} was likely related to the disruption of intermolecular hydrogen bonds in CT by the incorporated AC (Fig. S2B). XRD patterns indicated that both CT and CT/AC_5 showed characteristic diffraction peaks of CT at 2θ = 8.6° and 20°, suggesting that the introduction of AC did not alter the crystalline structure of CT. The appearance of a broad diffraction peak around 2θ = 25° in CT/AC_5, corresponding to AC, further confirmed the successful loading of AC (Fig. S2C).[29]

XPS analysis provided further evidence for interfacial interactions (Fig. 2I). The C 1s spectrum of pure CT could be

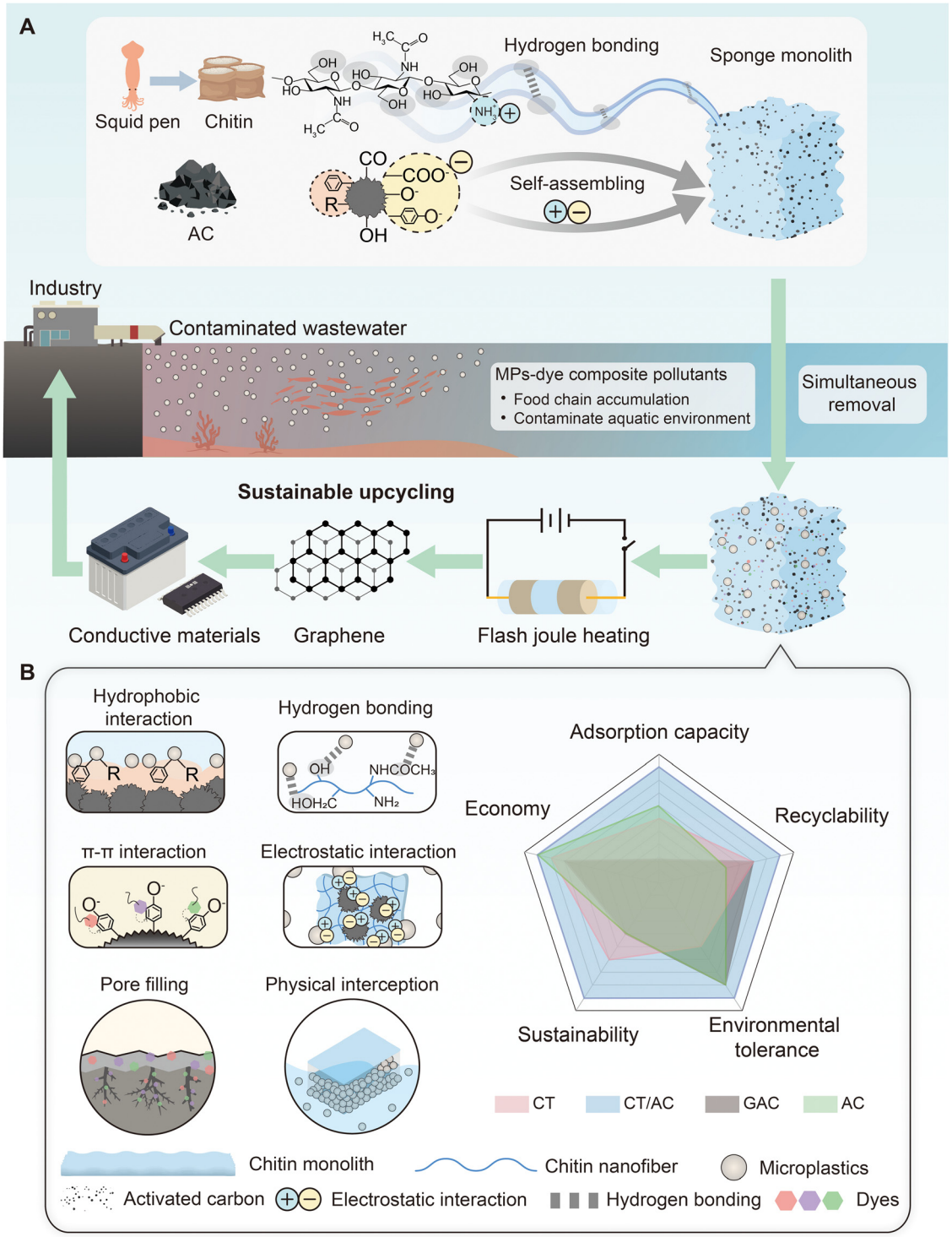

Fig. 1 From purification to upcycling: structure, mechanism, and comparative performance of the CT/AC sponge monolith. (A) Schematic diagram of the CT/AC sponge monolith's structure and upcycling process. (B) CT/AC sponge monolith's wastewater remediation mechanism and comparison of the performance factors of the CT/AC monolith with those of CT, granular AC (GAC), and AC (Table S1).

deconvoluted into three characteristic peaks at 284.80 eV (C–C), 286.40 eV (C–O/C–N), and 288.13 eV (C═O). A new peak emerged at 285.78 eV in CT/AC_5, attributable to the sp^2-hybridized graphitic carbon (C═C) from AC, providing direct evidence for successful compositing. The binding energy shift of the C–O/C–N peak indicated a decreased electron cloud

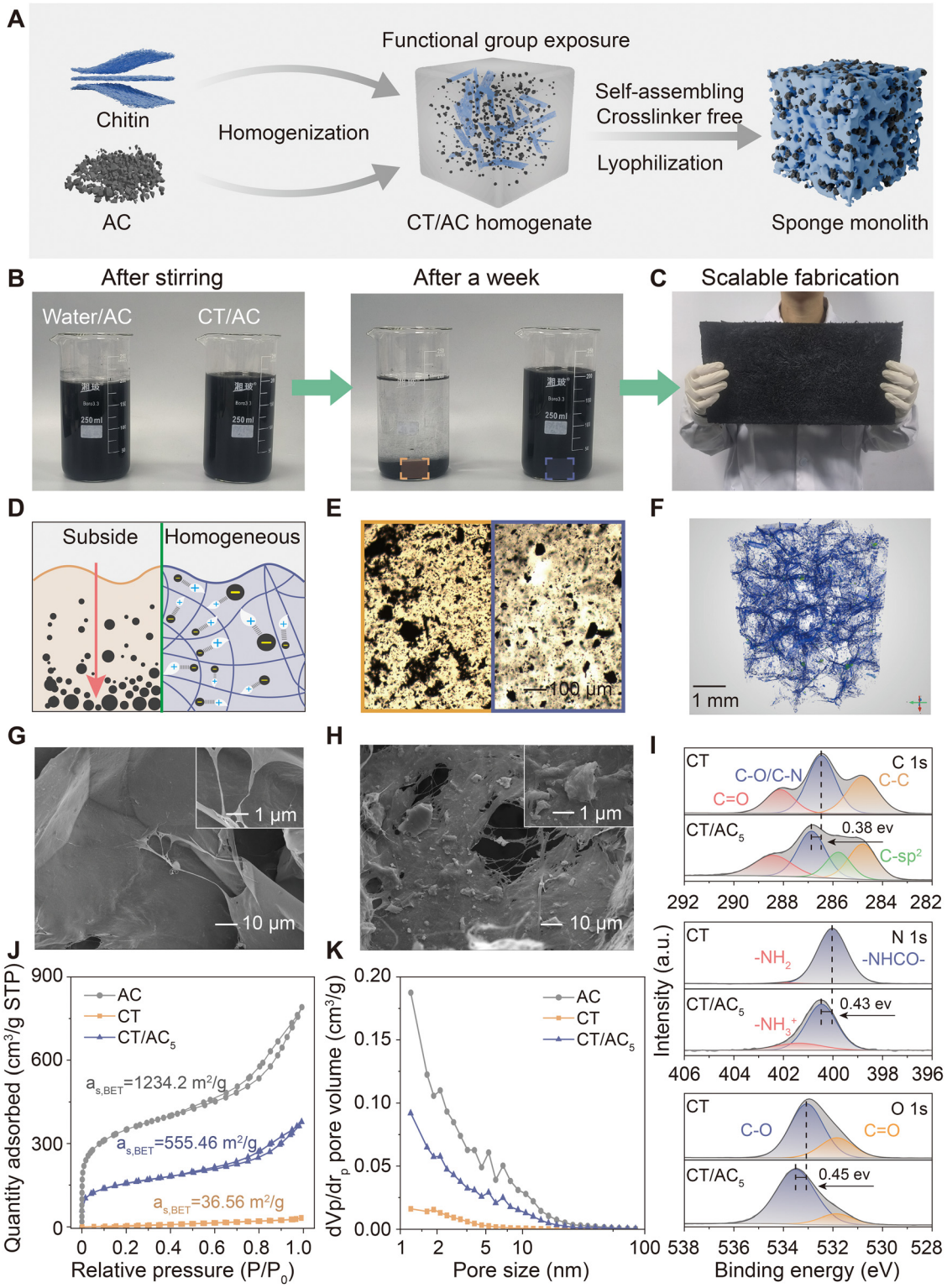

Fig. 2 Construction and characterization of CT/AC. (A) Pathway to fabricate a monolithic sponge from CT and AC without any crosslinking. (B) The photographs of the dispersion of AC in water (left) and the CT matrix (right). (C) Large sized monolithic sponge with a size of 30 × 50 cm^2. (D) Schematic diagram of the dispersion of AC in different media. (E) The microscopic images of AC in water (left) and the CT matrix (right). (F) XRM images of the CT/AC sponge. The SEM images of (G) CT and (H) CT/AC. (I) XPS spectra of C 1s, N 1s, and O 1s of CT and CT/AC_5. (J) The N_2 adsorption isotherms recorded at 77 K for the CT sponge and CT/AC_5. (K) The pore size distribution of CT and CT/AC_5.

density around the corresponding carbon atoms. In the N 1s spectrum, CT/AC_5 showed a significantly increased peak area for $-NH_3^+$ at 401.37 eV, with a lower binding energy compared to pure CT (402.01 eV), indicating enhanced protonation of $-NH_2$ groups on the CT chains, which strengthened the electrostatic interaction with AC.[19] In the O 1s spectrum, the shift of the C–O peak (533.05 eV) suggested a reduced electron density of the surface oxygen-containing functional groups of AC, potentially because they acted as binding sites at the interface.[30]

N_2 adsorption–desorption measurements quantitatively confirmed the successful integration of AC into the CT matrix (Table S2). The BET specific surface area increased markedly from 32.13 to 555.46 $m^2\ g^{-1}$ (CT/AC_5). Correspondingly, the adsorption–desorption isotherm transformed from type I to type II upon AC incorporation (Fig. 2J). The micropore volume (1–10 nm) also increased from 0.05 to 0.58 $cm^3\ g^{-1}$. This substantial enhancement, coupled with the preserved isotherm shape characteristic, demonstrated that the CT matrix did not block the intrinsic micropores of AC, thereby successfully maintaining AC's high-surface-area property (Fig. 2K).[31]

Robust performance of the CT/AC sponge monolith across different water matrices

CT slurry, as an excellent carrier for AC, can be easily molded into sponge-like materials with various geometric shapes through casting processes, such as different letters (Fig. 3A). The density of the CT/AC composite sponges increased progressively from 15.02 mg cm^{-3} for the pure CT sponge to 21 mg cm^{-3} with higher AC content (Fig. 3B). AC exhibits broad-spectrum pollutant removal capabilities due to its porous structure and abundant surface functional groups.[32] To systematically assess the enhancement effect of AC loading on the adsorption performance of the CT/AC composites, adsorption experiments were conducted using various dyes (*e.g.*, rhodamine B (RhB), malachite green (MG), and Congo red (CR)) as model pollutants, and the detailed parameters are listed in Table S3.[33–35] The adsorption results (Fig. 3C) showed that CT exhibited only limited adsorption capacity for PS and CR. In contrast, with increased AC content, the adsorption capacities of the CT/AC composite sponges for all types of dyes increased significantly, along with a notable expansion in the range of adsorbable pollutants, such as RhB, MG, CR, methylene blue (MB), methyl orange (MO), and crystal violet (CV). Specifically, the CT/AC_5 sponge achieved adsorption capacities of 898.33, 723.46, and 587.43 mg g^{-1} for RhB, MG, and CR, respectively, demonstrating exceptional adsorption performance. SEM images further revealed the adsorption mechanism at the microscopic scale; the adsorption of dyes resulted in a noticeably roughened material surface, suggesting coverage or binding of pollutant molecules on the fiber surfaces (Fig. S3).

Regarding the mechanism, the adsorption of dyes by AC primarily stemmed from the synergistic effect of physical adsorption and chemisorption involving its surface oxygen-containing functional groups (*e.g.*, hydroxyl and carboxyl groups) and well-developed pore structure. Conversely, the adsorption of CR by CT mainly relied on the strong electrostatic interaction between the protonated amino groups ($-NH_3^+$) on its molecular chains and the sulfonate groups ($-SO_3^-$) within the CR molecules. RhB, MG, and CR were selected as model dye pollutants to systematically evaluate the broad-spectrum adsorption performance of CT/AC_5. These dyes were representative in terms of charge properties (cationic, anionic, and zwitterionic) and molecular structure (Fig. S4).

Compression tests revealed a significant enhancement in mechanical properties with increasing AC loading. The compression strength of the pure CT sponge was merely 9.6 kPa, whereas the CT/AC_5 sponge achieved a strength of 38.06 kPa (Fig. 3D). This reinforcement effect was primarily attributed to the homogeneous dispersion of AC particles within the CT fibrous network, which acted as rigid support points during compression, effectively bolstering the mechanical integrity of the sponge material (Fig. 3E).

Owing to the inherent chemical inertness of both CT and AC, the CT/AC composite sponge demonstrated remarkable stability even in high-concentration acidic, alkaline, and saline solutions. To systematically evaluate its environmental tolerance, the cyclic compression performance of CT/AC_5 was tested in pure water, 10% HCl, 10% NaOH, and 3% NaCl solutions (Fig. 3F–I). The mechanical strength loss of the CT/AC_5 sponge was less than 30% after 100 compression cycles, while stable elasticity was consistently maintained. Additionally, after continuous shaking in the solutions at 140 rpm for 1 month (Fig. 3J), the sponge retained its structural integrity with minimal mass loss (Fig. 3K), convincingly confirming its excellent structural durability and component stability under complex and harsh conditions.

Efficient dual-target removal of microplastics and dyes by the CT/AC sponge monolith

To reflect the diversity of environmental microplastics, fluorescently labeled PS microspheres of varying sizes were used as model pollutants to assess the adsorption preference of the CT/AC_5 composite. A significant difference in adsorption capacity was observed, with 5 μm PS (1249.41 mg g^{-1}) being much more effectively adsorbed than 100 nm PS (246.42 mg g^{-1}) (Fig. 4A). In conjunction with the BET analysis of CT/AC_5 and the zeta potential data for PS of different sizes (Fig. S5), pore size matching emerges as the primary mechanism underlying the size-dependent adsorption behavior. This is directly evidenced by SEM images (Fig. 4B and C), which reveal the successful and uniform entrapment of PS within the fibers of CT/AC_5, underscoring the essential function of its hierarchical pore structure.[36] Consequently, 5 μm PS was chosen as the model pollutant for further study. The adsorption capacity of CT/AC_5 exhibited a strong concentration dependence, increasing from 341.29 to 1231.55 mg g^{-1} as the PS concentration increased from 100 to 500 mg L^{-1} (Fig. 4D). Notably, even at a concentration close to real environmental levels, the removal rate remained as high as 92%–98.76%, confirming its feasibility for practical remediation (Fig. S6).[37] Similarly, the adsorption of RhB, MG, and CR dyes also increased significantly with

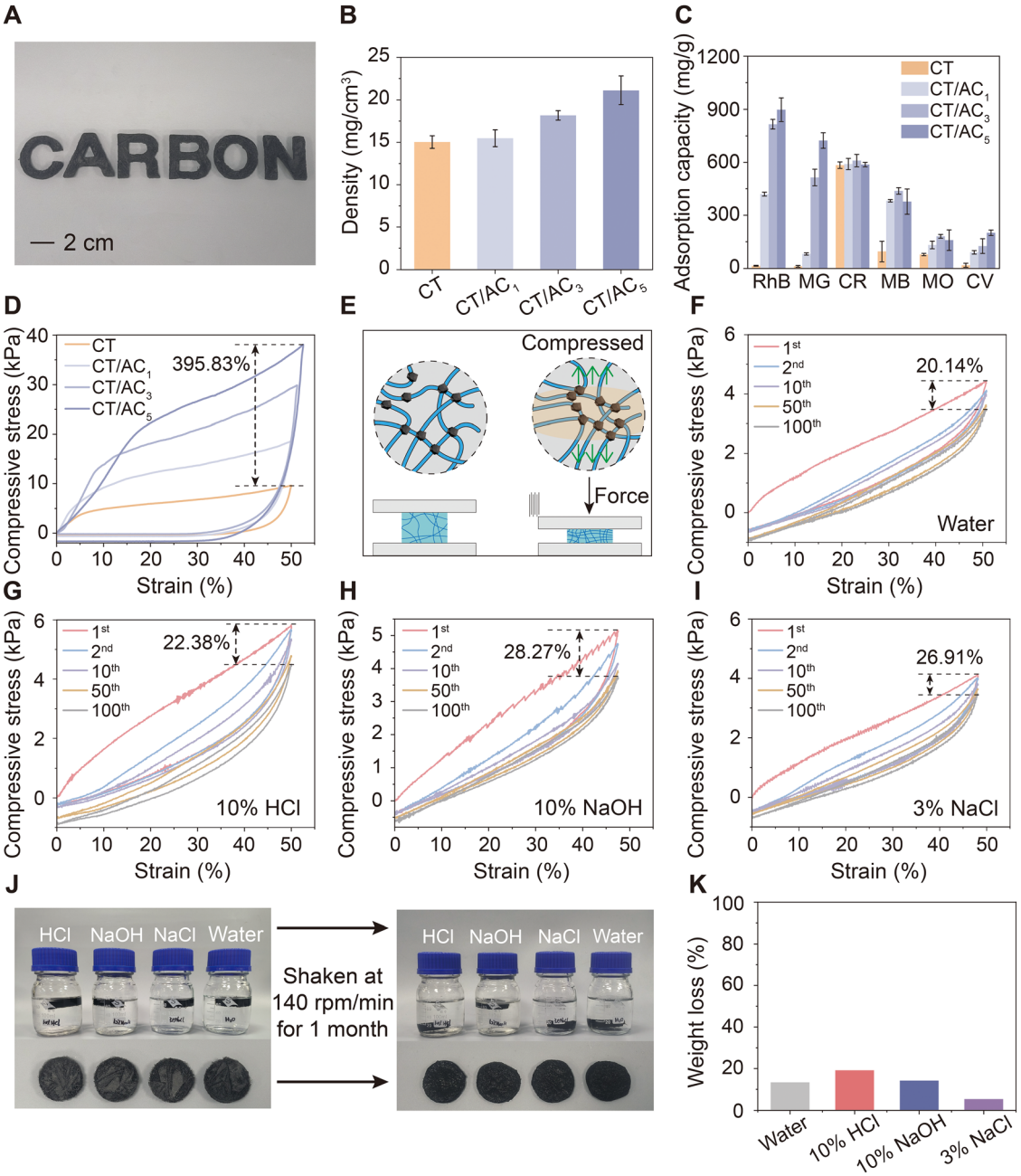

Fig. 3 Performance comparison and screening of sponge monoliths with different dosages of AC. (A) The image of a sponge monolith in various shapes. (B) The density of CT/AC sponges with varying AC content, alongside (C) adsorption capacity for multiple dyes (RhB, MG, CR, MB, MO, and CV). (D) The compression stress–strain curves of CT, CT/AC_1, CT/AC_3, and CT/AC_5. (E) Schematic diagram of the compression of the CT/AC_5 sponge structure. Cyclic compression performance of CT/AC_5 in (F) water, (G) 10% HCl, (H) 10% NaOH, and (I) 3% NaCl. (J) Photographs and (K) weight loss of CT/AC_5 after shaking in 10% HCl, 10% NaOH, 3% NaCl, and water (150 rpm min^{-1}) for 1 month at 298 K. The sponges still maintained their original appearance after shaking for 1 month, and their weight loss was <20%. Error bars represent the standard deviation (n = 3).

higher initial concentrations (50 to 300 mg L^{-1}), reaching capacities of 1115.41, 821.00, and 702.68 mg g^{-1}, respectively (Fig. 4E). This concentration-dependent performance, coupled with excellent retention of efficiency at high pollutant loads, underscores the strong potential of CT/AC_5 for treating heavily contaminated wastewater.

The adsorption kinetics is shown in Fig. 4F. The adsorption capacity increased rapidly within the initial 60 minutes for all systems and reached equilibrium within 48 h. Kinetic modeling indicated that the adsorption of PS and MG better followed the pseudo-first-order model (Table S4), suggesting a physisorption-dominated process, such as pore filling and surface deposition, whereas the adsorption of RhB and CR better conformed to the pseudo-second-order model, implying chemisorption mechanisms, such as surface complexation, electrostatic attraction, and chemical bonding (Fig. 4G and H). The

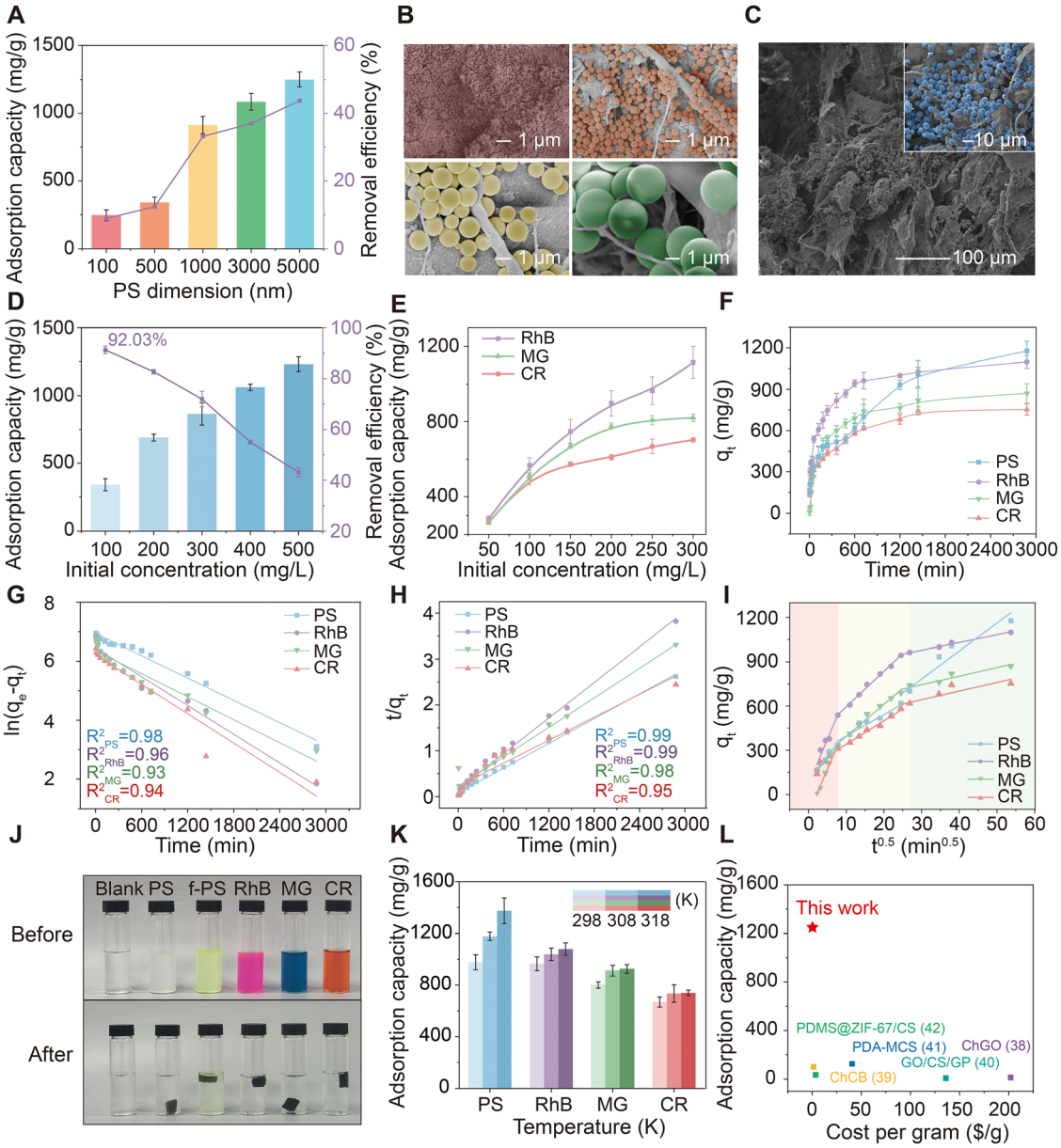

Fig. 4 Adsorption performance of the CT/AC_5 sponge monolith for different pollutants. (A) Adsorption capacity of CT/AC_5 for PS microspheres at different dimensions and SEM images of the CT/AC_5 sponge after the capture of (B) 100, 500, 1000, 3000, and (C) 5000 nm PS particles (colored regions representing microplastics). Adsorption capacity of CT/AC_5 for (D) PS microspheres and (E) dyes (RhB, MG, and CR) at different initial concentrations. (F) Adsorption capacity of CT/AC_5 for PS microspheres and dyes (RhB, MG, and CR) at different times. Adsorption kinetics fitted by the (G) pseudo-first-order model, (H) pseudo-second-order model, and (I) intra-particle diffusion model for adsorption of PS microspheres, RhB, MG, and CR on $CTAC_5$. Images of different pollutants before and after treatment with CT/AC_5. (J) Images of different pollutants before and after treatment with CT/AC_5. (K) Adsorption capacity of CT/AC_5 for PS microspheres and dyes (RhB, MG, and CR) at different temperatures. (L) Comparison of CT/AC_5 and other reported chitin/chitosan materials including ChGO, ChCN, ChCB, PDA-MCS, GO/CS/GP, and PDMS@ZIF-67/CS.[38–42] Error bars represent the standard deviation (n = 3).

intraparticle diffusion model revealed a multi-stage adsorption process for all pollutants (Fig. 4I). For 5 μm PS microspheres, the later stage showed a significantly faster diffusion rate, confirming a shift to volumetric capture within the macropores of the sponge. In contrast, the dye pollutants exhibited rapid initial surface adsorption followed by slower internal diffusion stages (Table S5).

The visual outcome of the adsorption experiments was striking (Fig. 4J). The original pollutant solutions became nearly clear after shaking, providing intuitive evidence of efficient removal capability for various pollutants of CT/AC_5. The original solutions of green-fluorescent PS microspheres and auto-fluorescent RhB showed strong fluorescence under UV light, which was largely diminished after adsorption, indicating effective capture of the pollutants (Fig. S7). To investigate the thermodynamics of the adsorption process, adsorption experiments were conducted at different initial concentrations and temperatures of 298, 308, and 318 K (Fig. 4K).

The equilibrium adsorption capacities of CT/AC_5 for all target pollutants (PS, RhB, MG, and CR) increased with increasing temperature, exhibiting characteristics of an endothermic process. Specifically, at an initial concentration of 500 mg L^{-1}, the adsorption capacity for PS increased from 977.41 mg g^{-1} at 298 K to 1204.72 mg g^{-1} at 318 K, that for RhB increased from 964.97 to 1079.51 mg g^{-1}, that for MG increased from 800.70 to 925.29 mg g^{-1}, and that for CR increased from 668.30 to 739.86 mg g^{-1}, indicating that heating favored the adsorption process. The adsorption of all pollutants at various temperatures conformed to the Langmuir model (Fig. S8 and Tables S6 and S7), suggesting that adsorption occurred primarily as a monolayer on homogeneous surfaces. The adsorption capacities of CT/AC_5 for PET and PMMA were 792.99 and 1081.83 mg g^{-1}, respectively (Fig. S9). Overall, owing to the self-assembly between CT fibers and AC powders without cross-linking, CT/AC_5 exhibited both outstanding cost efficiency and high microplastic adsorption capacity, outperforming most existing chitin/chitosan-based sponges (Tables S8 and S9).[38–42] Furthermore, due to its simple raw materials and straightforward preparation process, it offered significant cost advantages (Fig. 4L).

In nature, microplastics act as carriers for dyes, facilitating the co-migration and spread of pollutants.[7,43] The synergistic removal capability of the CT/AC_5 sponge for dye–microplastic (PS) binary composite pollution systems is crucial. The presence of dyes caused competitive inhibition for PS adsorption. In the RhB/PS, MG/PS, and CR/PS systems, the adsorption capacity for PS decreased from 1231.55 to 632.78, 422.42, and 282.73 mg g^{-1}, respectively (Fig. 5A). Notably, the anionic dye CR showed the strongest competitive adsorption, leading to the most significant reduction in PS uptake. In contrast, the adsorption capacities of the three dyes in the binary systems (1058.81, 800.70, and 593.89 mg g^{-1} for RhB, MG, and CR, respectively) remained largely comparable to their respective capacities when adsorbed alone (1079.51, 783.23, and 668.30 mg g^{-1} for RhB, MG, and CR, respectively), indicating that CT/AC_5 was able to effectively remove dye pollutants even in complex pollution systems (Fig. 5B–D). To better simulate real-world conditions, the interference of common co-existing substances such as metal ions (Na^+, Mg^{2+}, and Ca^{2+} at 30 ppm), SiO_2 nanoparticles (250 ppm), and humic acid (HA) (30 ppm) was further investigated. Na^+ and Mg^{2+} significantly inhibited PS adsorption in the MG/PS system. Interestingly, in the RhB/PS system with Ca^{2+} ions present, SEM images revealed crystal formation on the PS surface, speculated to be chelates formed between Ca^{2+} ions and the carboxyl groups of RhB. Nano-SiO_2 adsorbed onto the PS surface and clogged AC pores, thereby generally suppressing the adsorption of both PS and dyes, and HA primarily affected MG adsorption (Fig. S10). Overall, CT/AC_5 maintained stable adsorption of dyes across various complex scenarios, and its adsorption of PS remained effective in most cases.[24]

The influence of pH was assessed by adjusting the initial solution pH (3–11) using 1 mM HCl or NaOH under conditions of 298 K and 24 h. The results showed that the adsorption capacity of CT/AC_5 for PS gradually decreased as the pH increased from 3 to 9 (Fig. 5E). CT/AC_5 maintained stable and high adsorption capacities for various dyes across the entire pH range, indicating strong pH adaptability. The effect of ionic strength was evaluated by adding NaCl. As the concentration increased from 0.0001 to 1%, the adsorption capacity of CT/AC_5 for PS decreased significantly from 1194.07 to 477.63 mg g^{-1}, likely due to the weakened electrostatic attraction. For the dye pollutants, the adsorption capacities of RhB and MG remained stable across different salt concentrations. However, the adsorption capacity for CR, an anionic dye, increased from 663.82 to 958.51 mg g^{-1}, which may be attributed to the introduction of AC further increasing the surface area of CT, thereby providing additional adsorption sites for CR (Fig. 5F).

To evaluate the broad-spectrum adsorption performance of CT/AC_5 toward environmentally relevant microplastics, we further tested its affinity for several common types of microplastics. We selected PS, polyethylene (PE), polypropylene (PP), polyethylene terephthalate (PET), and polymethyl methacrylate (PMMA), all with micron-sized particles (Fig. S11). As shown in Fig. 5G, CT/AC_5 exhibited substantial adsorption capacities for all types microplastics, with the performance from 291 to 577.83 mg g^{-1}. The differences in adsorption capacity might be related to the surface chemistry of the microplastics themselves and the strength of their interfacial interaction with the adsorbent. Furthermore, benefiting from the rich π-electron system provided by the AC component, CT/AC_5 also showed good affinity for typical organic micropollutants. Its adsorption capacities for ibuprofen and bisphenol A reached 93.55 and 147.52 mg g^{-1} (Fig. S12). According to DFT calculations, the adsorption of CT/AC_5 onto PS-RhB was governed by electrostatic and π–π interactions, whereas π–π interactions prevail for PS-MG, and electrostatic interactions played the dominant role for PS-CR (Fig. 5H and Fig. S13). To simulate real water remediation scenarios, CT/AC_5 was packed into a fixed-bed adsorption setup (20 cm height). Its synergistic removal performance for low-concentration pollutants (20 ppm each for PS and dyes) was evaluated under dynamic flow conditions (Fig. 5I and Table S10).[44] CT/AC_5 achieved removal rates exceeding 95% in the vast majority of dynamic adsorption processes for binary pollutants, as clearly demonstrated by the before-and-after comparison in the optical photographs (Fig. 5J).

Life cycle assessment and end-of-life upcycling of the sponge monolith

Based on the environmental impact of adsorbent consumption per unit amount of pollutant treated, a life cycle assessment (LCA) of CT/AC_5 and GAC was conducted. The ReCiPe 2016 Midpoint (H) method was used (Table S11). This method categorizes environmental impacts into 18 categories, systematically assessing the environmental load of each process by quantifying emissions of various harmful substances.[45,46] The LCA boundary spanned from the extraction of squid bones to the purification of CT, culminating in the final product preparation (Fig. 6A and Fig. S14).[47] The functional unit was defined as the production process of the adsorbent required to achieve the adsorption of 1 kg microplastics. Under an

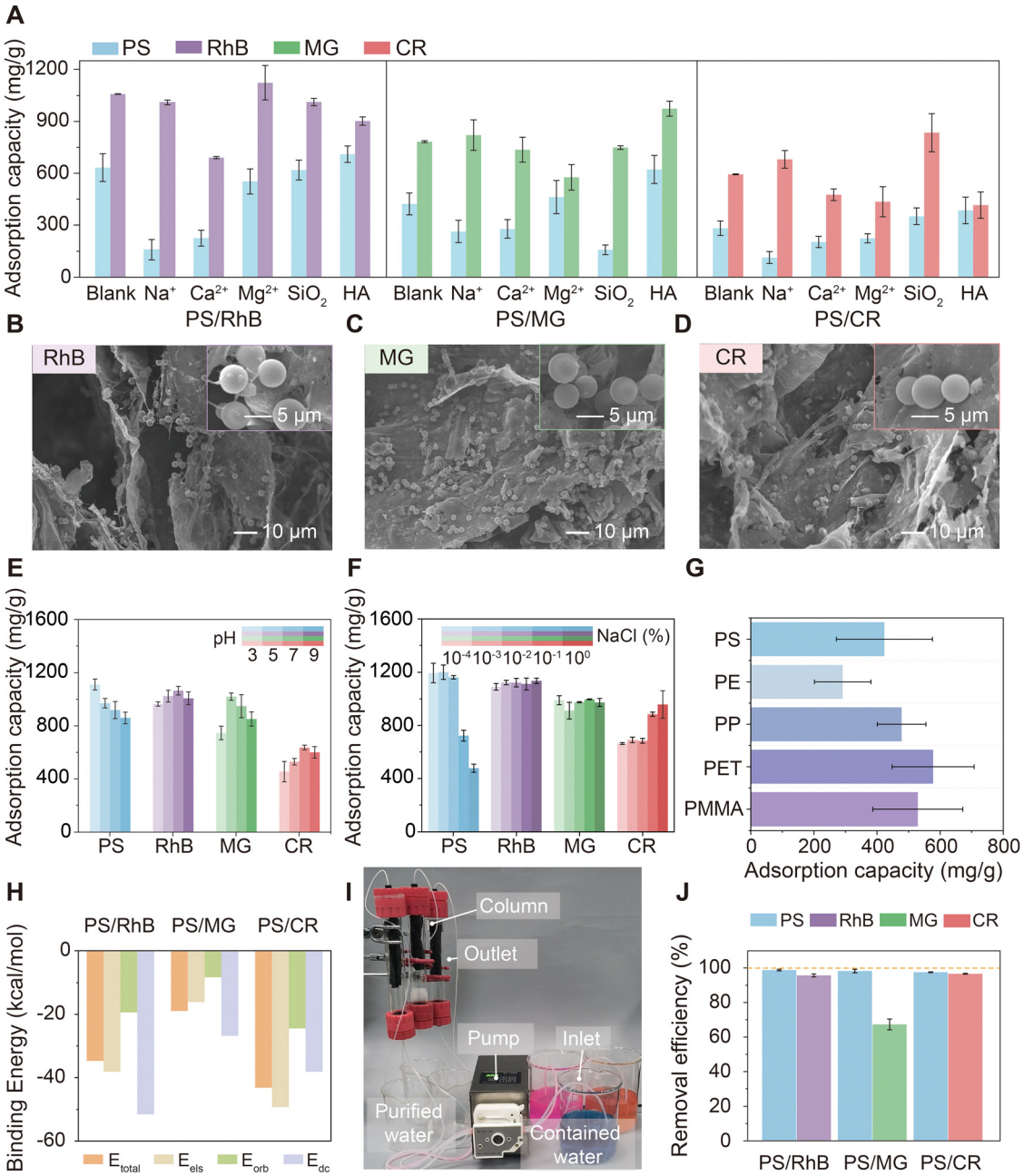

Fig. 5 Binary adsorption performance of CT/AC_5. (A) Binary adsorption capacity of CT/AC_5 for PS/dyes under different conditions (30 ppm Na^+, Ca^{2+}, Mg^{2+}, and humic acid, and 250 ppm SiO_2). SEM images of CT/AC_5 for adsorption of (B) PS/RhB, (C) PS/MG and (D) PS/CR binary pollutants. Adsorption capacity of CT/AC_5 for PS microspheres and dyes (RhB, MG, and CR) at different (E) pH values and (F) salt concentrations. (G) Adsorption capacity of CT/AC_5 for ambient plastic particles. (H) Theoretical binding energies of CT/AC_5 toward different PS and dyes. (I) Optical photograph of a simplified benchtop water treatment device to purify PS/dye-containing water (20 ppm of both dye and microplastics). (J) Removal efficiency of PS/dyes in water.

identical dosing mass (0.01 g), the adsorption capacity of CT/AC_5 for pollutants was significantly superior to that of GAC (Fig. 6B). The adsorption capacity of GAC for PS microplastics was only 2.43 mg g^{-1}. Its capacities for RhB, MG, and CR were also relatively low at 4.10, 14.86, and 4.77 mg g^{-1}, respectively. In contrast, the adsorption capacity of CT/AC_5 for PS was approximately 400 times that of GAC. Its capacity for dyes was 60–200 times greater (Fig. 6C).[48]

Using the treatment of 1 kg microplastics as the evaluation benchmark, the LCA results indicated that CT/AC_5 outperformed the traditional AC across all 18 environmental impact indicators (Fig. 6D). Significant reductions were observed in key indicators. These included global warming potential (GWP, −59%), fossil resource scarcity (FFP, −68%), terrestrial acidification potential (TAP, −72%), and fine particulate matter formation potential (PMFP, −68%). Substantial reductions

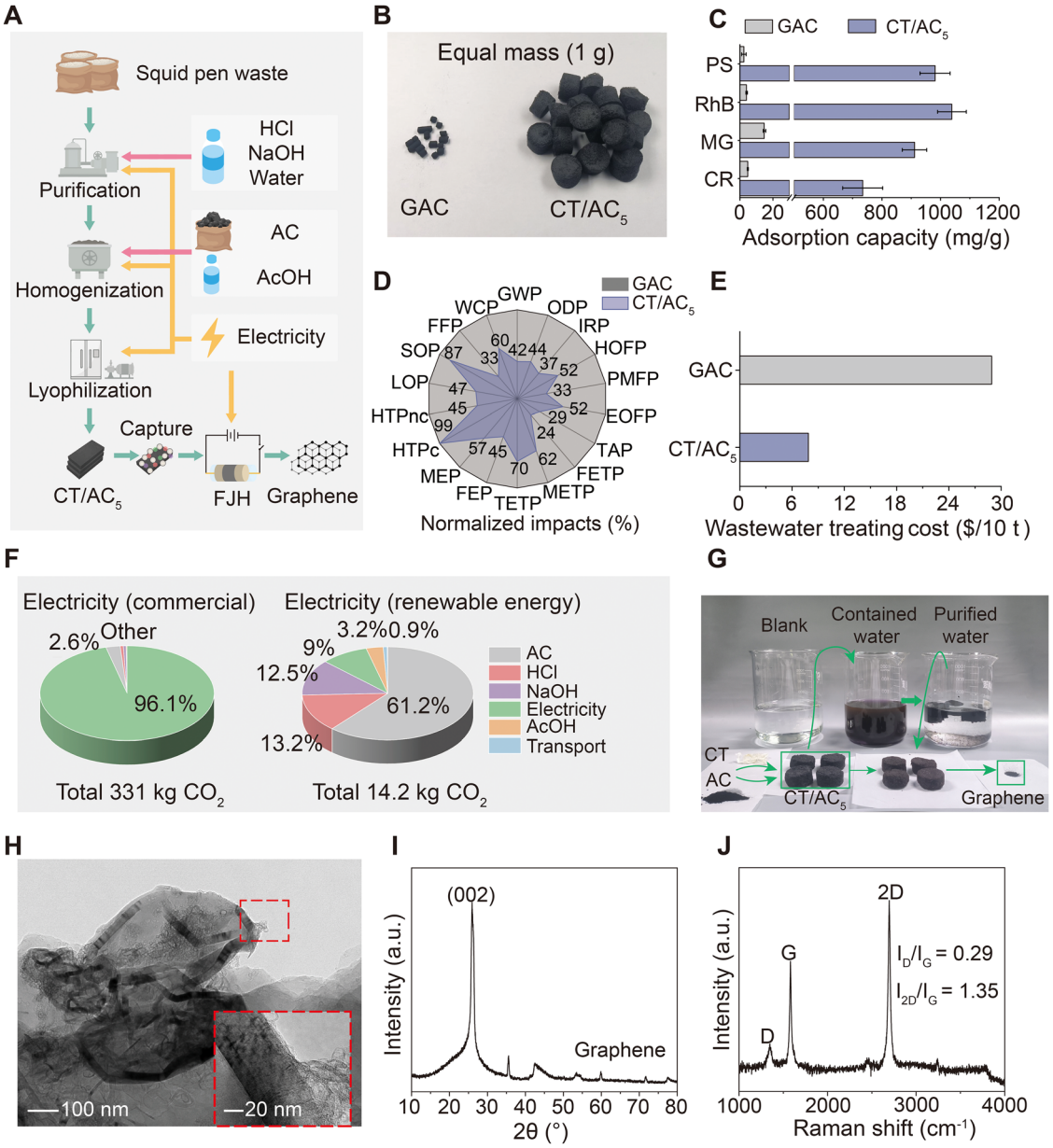

Fig. 6 LCA and upcycling of CT/AC_5. (A) Schematic diagram of the CT/AC_5 production and upcycling process. (B) Optical photograph of GAC and CT/AC with an equal mass (1 g). (C) Comparison of adsorption capacities for pollutants between GAC and CT/AC. (D) LCA comparison of GAC and CT/AC_5 for treating pollutants of the same unit (1 kg). (E) The cost incurred for treating 10 t wastewater containing microplastics. (F) CO_2 footprint distribution from producing 1 kg CT/AC_5 using electricity from different sources. (G) Raw materials, sponge, graphene, and visual demonstrations before and after wastewater treatment. The (H) TEM, (I) XRD and (J) Raman spectra of graphene produced by FJH after CT/AC_5 adsorbed pollutants. GWP: global warming potential, WCP: water consumption potential, FFP: fossil resource scarcity, SOP: surplus ore potential, LOP: land occupation potential, HTPnc: human non-carcinogenic toxicity potential, HTPc: human carcinogenic toxicity potential, MEP: marine eutrophication potential, FEP: freshwater eutrophication potential, TETP: terrestrial ecotoxicity potential, METP: marine ecotoxicity potential, FETP: freshwater ecotoxicity potential, TAP: terrestrial acidification potential, EOFP: photochemical oxidant formation potential: ecosystems, PMFP: particulate matter formation potential, HOFP: photochemical oxidant formation potential (human), IRP: ionizing radiation potential, ODP: ozone depletion potential. Error bars represent the standard deviation (n = 3).

ranging from 40% to 70% were also achieved in multiple other categories. Examples include ionizing radiation potential (IRP, −64%), freshwater eutrophication potential (FEP, −77%), and human non-carcinogenic toxicity potential (HTPnc, −55%). This comprehensive environmental advantage primarily stemmed from the exceptional adsorption capacity of CT/AC_5. Compared to conventional AC, it required significantly less material to treat the same amount of pollutants.

Beyond its exceptional adsorption performance, the CT/AC_5 sponge was designed with end-of-life sustainability in mind. To transition from "adsorb-and-dispose" to a circular economy framework, we employed FJH to convert contaminant-rich

spent adsorbents into high-value graphene. Crucially, the embedded AC served as an ideal carbon source. Meanwhile, the CT-derived carbon framework provided structural continuity. These components jointly enabled this transformation process.[49–51] Therefore, when treating 10 tons of identical microplastic wastewater, CT/AC_5 demonstrated lower overall costs compared to GAC (Fig. 6E). As shown in Fig. 6F, when using commercially available electricity to produce CT/AC_5, the power consumption accounted for a significant portion of the energy input. However, when utilizing renewable energy sources, the carbon footprint decreased from 331 to 14.2 kg CO_2 eq. The production process of CT/AC_5 was convenient and environmentally friendly, with raw materials being widely available and easily accessible. It holds promising prospects for the future as the proportion of renewable energy continues to increase.

The entire high-value conversion process started from raw materials and went to the synthesis of the CT/AC_5 and its subsequent conversion into graphene after water treatment (Fig. 6G). The resulting product exhibited graphene-like morphologies, characterized by translucent sheets with distinctive wrinkles (Fig. 6H), indicating the formation of few-layer graphene with structural integrity. The graphitized structure was confirmed by XRD, which showed a distinct (002) diffraction peak (Fig. 6I). Furthermore, Raman spectroscopy corroborated the high crystallinity, evidenced by a low I_D/I_G ratio of 0.29 and an I_{2D}/I_G ratio of 1.35, accompanied by a sharp 2D peak profile, which was characteristic of few-layer graphene (Fig. 6J). FJH successfully upcycles spent adsorbent into high-quality graphene, enabling a closed-loop lifecycle for sustainable adsorbent management.

Conclusion

In summary, we have developed a mechanically robust and reusable chitin/activated carbon (CT/AC) sponge monolith *via* a proton-assisted self-assembly strategy, which integrated powdered AC uniformly into a porous CT matrix to create a high-performance dual-target adsorption system. The material exhibited outstanding adsorption capacities for individual pollutants, reaching 1177.17 mg g^{-1} for 5 μm PS microspheres, and 1038.86, 911.23, and 734.47 mg g^{-1} for RhB, MG, and CR, respectively. More importantly, in complex binary systems containing both microplastics and dyes, the sponge achieved effective simultaneous removal, underscoring its capability for treating multi-component effluents. This high efficiency may arise from the synergistic mechanisms of pore filling, physical interception, electrostatic interaction, hydrophobic interaction, hydrogen bonding, and π–π interaction. The sponge maintains high removal efficiency across broad pH ranges and under high ionic strength, while demonstrating excellent mechanical stability over 100 compression cycles under harsh conditions. Furthermore, end-of-life management through FJH upcycles the spent adsorbent into graphene, enabling a circular economy approach that avoids secondary pollution and transforms waste into value-added products. This work presents a sustainable and scalable strategy for high-performance, dual-target water remediation.

Materials and methods

Materials

Activated carbon (400 mesh) and granular activated carbon were purchased from Macklin Co., Ltd (Shanghai, China). Chemical reagents of analytical purity (AR), namely acetic acid, hydrochloric acid, sodium hydroxide, sodium chloride, rhodamine B, malachite green, Congo red, methylene blue, methyl orange, crystal violet, and ethanol, were purchased from Sinopharm Chemical Reagent Co., Ltd (China). PS, PE, PP, PET, and PMMA particles with a random diameter of 1–3 μm were purchased from Kexinda Polymer Material Co., Ltd (Shanghai, China). Fluorescent PS microspheres with diameters of 100, 500, 1000, 3000, and 5000 nm (excitation wavelength: 540 nm, emission wavelength: 580 nm) were purchased from Dae Technology Co., Ltd (Tianjin, China). PET and PMMA microplastics were acquired from Bioty Science Biotechnology Co., Ltd, China. All aqueous solutions were prepared using ultrapure water with a resistance of 18.2 MΩ cm.

Preparation of CT/AC_5 sponges

Chitin flakes were added to 0.2% acetic acid and soaked for 24 h, then homogenized using a soymilk machine (SP902S, Supor, China) for 10 minutes to obtain a 0.5 wt% chitin (CT) homogenate. At this point, a certain mass of activated carbon and the chitin homogenate were added together into a soymilk machine and stirred for 10 min to obtain the CT/AC mixture. The CT/AC mixture was poured into a mold and frozen. The frozen samples were freeze-dried under vacuum for 24 h to obtain CT/AC sponges. When the content of activated carbon in the system was 0, 0.1, 0.3, and 0.5 wt%, the sponges were denoted as CT, CT/AC_1, CT/AC_3, and CT/AC_5, respectively.

Characterization

Optical photographs involved in the whole experiment were acquired using a camera. The morphology of sponges before and after NP removal was observed using a field emission scanning electron microscope (FE-SEM, Zeiss SIGMA, Germany) and an inverted microscope (Motic AE2000, China). Zeta potential was measured using a Zetasizer (Zetasizer Nano ZSP, UK). FTIR spectra were recorded in the ATR mode using a Nicolet iS20 (Thermo Scientific, USA) to obtain information about chitin functional group interactions. The C, N and O surface elements of the samples (crushed into powder) were detected by XPS (Kratos, UK). XRD patterns of the samples were collected using a type D/max-rA diffractometer (Bruker D8 Advance, Germany), with a Cu target and Kα radiation (λ = 0.154 nm) at 40 kV over an angular (2θ) range of 5–60°. The mechanical behavior of the sponges was measured using a universal testing machine (CMT6350, Shenzhen SANS Test Machine Co., Ltd China) at a constant compression rate of

1 mm s^{-1}. The microstructure of the sponges was observed using 3D Micro-CT (Bruker Skyscan1272, German). The specific surface area (BET model) and pore size distribution (BJH model) were determined from nitrogen adsorption–desorption isotherms obtained using a TriStar II 3020 analyzer (USA). The FJH treatment was performed using an FJH-2025Aplus instrument (Sine Joule Heating Co, China).

Adsorption capacity

A series of experiments were conducted to demonstrate the universal adsorption capacity of CT/AC sponges. Each experiment was conducted by agitating the cylindrical CT/AC sponges (approximately 3.5 mg, 6 mm in diameter, and 10 mm in height) at 150 rpm min^{-1} in a thermostatic shaker incubator (SHZ-82, ZBR, China) until adsorption equilibrium was reached. A fluorescence spectrophotometer (FS5, Edinburgh, UK) was used to measure the change in the fluorescence intensity of fluorescent PS in the solution before and after adsorption. UV-vis spectroscopy was used to measure the characteristic absorption peaks of dyes to reflect the change in dye concentration in the solution before and after adsorption. The concentration of pollutants was calculated from the standard curve function. The adsorption capacity of CT/AC sponges was calculated using the following equation:

$$\text{Adsorption capacity } (Q) = \frac{(\gamma_0 - \gamma) \times V}{m}$$

where Q (mg g^{-1}) is the uptake of pollutants per unit mass of sponges, γ_0 and γ (mg mL^{-1}) are the initial concentration and equilibrium concentration of the pollutant in the aqueous solution, respectively, V (mL) is the volume of the aqueous solution, and m (g) is the weight of the foams.

The universality of the CT/AC_5 sponge was evaluated by the adsorption of multiple microplastic particles. Firstly, 500 ppm of PS, PP, PE, PET and PMMA particles were suspended in 0.05 g L^{-1} of Tween 80. Next, the CT/AC_5 sponge (approximately 3.5 mg, 6 mm in diameter, and 10 mm in height) was added to 20 mL of microplastic suspensions separately and then shaken at 150 rpm min^{-1} for 24 h at 298 K. Finally, the CT/AC_5 sponge after adsorption was rinsed with water, and the dried sponge was weighed carefully using a precision balance (124-1CN, Sartorius, Germany). The adsorption capacity was calculated using the following equation:

$$\text{Adsorption capacity } (Q) = \frac{(m_1 - m_0)}{m_0} \times 1000$$

where Q (mg g^{-1}) is the uptake of microplastics per unit mass of sponges and m_0 and m_1 (g) are the weights of the foams before and after adsorption, respectively.

DFT calculations

All DFT calculations were performed using Gaussian 09 software. Geometry optimizations were carried out with the IEFPCM implicit solvation model to simulate the aqueous solution environment. Binding energies were calculated and the basis set superposition error (BSSE) was taken into account and corrected. The energy decomposition analysis was performed using the sobEDA program. The grid data for the independent gradient model based on Hirshfeld partition (IGMH) isosurface maps were computed using Multiwfn software and visualized with VMD.

LCA

A life cycle assessment was conducted in accordance with ISO 14 040 and ISO 14 044 standards. The goal of this assessment was to quantify the environmental impacts associated with the production of the CT/AC_5 monolithic adsorbent using a cradle-to-gate system boundary. This includes raw material acquisition, processing, and all fabrication steps up to the final material at the factory gate. The life cycle inventory was compiled primarily from experimental data, detailing material and energy inputs for each stage of sponge synthesis, as provided in Table S11. Process by-products were accounted for as waste streams and assigned appropriate recovery and treatment pathways. The impact assessment was performed using SimaPro 9.0 with the ecoinvent v3 database. The ReCiPe 2016 Midpoint (H) method was employed, enabling evaluation across eighteen categories of environmental impact. To align with the materials adsorption function and facilitate meaningful comparison, the functional unit was defined as the production of sufficient adsorbent to remove 1 kg of microplastic.

FJH

RhB, MG, CR, and PS (each at 20 ppm) were dissolved in 500 mL of deionized water to simulate wastewater containing multiple dyes. 2.0 g of the CT/AC_5 adsorbent was added to the wastewater, then the reaction beaker was placed on a shaking platform and shaken for 24 h at 80 rpm and 25 °C.

After adsorption, the adsorbed CT/AC_5 sample was obtained through freeze-drying under vacuum. 0.28 g of the adsorbed CT/AC_5 sample were placed in the quartz tube of a Joule heating apparatus (FJH-2025Aplus, Sine, China). Under an air atmosphere, the sample was pre-treated at 1200 °C for 50 s, followed by flash vaporization: first five flash vaporizations were performed at 60 V for 0.5 s each, then the voltage was increased to 180 V for a 0.5 s flash vaporization, ultimately increasing the sample temperature above 3600 °C. After processing, a total of 0.04 g of the final sample was obtained.

Statistical analysis

All experiments were performed in triplicate, and the results were presented as mean values ± standard deviations (n = 3).

Author contributions

Ting Huang and Yang Wu conceived the concept. Hongbing Deng and Xue Zhou supervised the project. Ting Huang, Fangtian Liu, and Yifei Liu conducted the experiments. Yang Wu and Xiaowen Shi provided valuable suggestions on data analysis and manuscript preparation. Ting Huang, Yang Wu,

and Fangtian Liu wrote the manuscript. Hongbing Deng and Yang Wu were responsible for funding acquisition. All authors discussed the results and contributed to the editing and revision of the manuscript.

Conflicts of interest

There are no conflicts to declare.

Data availability

The data that support the findings of this study are available from the corresponding authors Yang Wu, Hongbing Deng, and Xue Zhou upon reasonable request.

Supplementary information (SI) includes additional physicochemical characterization of CT/AC (including SEM, FTIR, Raman, and XRD) and additional adsorption performance for dyes and microplastics. In addition, reference data for performance comparison radar charts are provided, listing the adsorption kinetics, isotherms, and thermodynamic parameters of CT/AC for microplastics and dyes. The process parameters related to life cycle assessment (LCA) are also supplied. See DOI: https://doi.org/10.1039/d6mh00083e.

Acknowledgements

We thank the Test Center and Core Facility of Wuhan University for assistance with material characterization, with special appreciation to Dr Yu Zhang for her expert assistance with X-ray microscopy (XRM) analysis. This work was supported by the National Natural Science Foundation of China (No. 52373062, 52573122, 52173061 and 52203069) and the Fundamental and Interdisciplinary Disciplines Breakthrough Plan of the Ministry of Education of China (No. JYB2025XDXM402).

References

1 J. Lin, W. Ye, M. Xie, D. H. Seo, J. Luo, Y. Wan and B. Van der Bruggen, *Nat. Rev. Earth Environ.*, 2023, **4**, 785–803.
2 R. C. Thompson, W. Courtene-Jones, J. Boucher, S. Pahl, K. Raubenheimer and A. A. Koelmans, *Science*, 2024, **386**, eadl2746.
3 C. M. Rochman, *Science*, 2018, **360**, 28–29.
4 S. ten Hietbrink, D. Materić, R. Holzinger, S. Groeskamp and H. Niemann, *Nature*, 2025, **643**, 412–416.
5 M. S. Bank, D. M. Mitrano, M. C. Rillig, C. Sze Ki Lin and Y. S. Ok, *Nat. Rev. Earth Environ.*, 2022, **3**, 736–737.
6 J. Woodward, J. Li, J. Rothwell and R. Hurley, *Nat. Sustain.*, 2021, **4**, 793–802.
7 Y. Duan, S. Y. Sun, J. Zhao and H. Yuan, *Sep. Purif. Technol.*, 2025, **359**, 130505.
8 L. Chen, C. Mao, S. Yuan, X. Pu, H. Liang, X. Chen, H. Shao and M. Wu, *Chem. Eng. J.*, 2024, **502**, 157915.
9 V. K. Sharma, X. Ma, E. Lichtfouse and D. Robert, *Environ. Chem. Lett.*, 2023, **21**, 1933–1936.
10 S. Allen, D. Allen, V. R. Phoenix, G. Le Roux, P. Durántez Jiménez, A. Simonneau, S. Binet and D. Galop, *Nat. Geosci.*, 2019, **12**, 339–344.
11 T. S. Galloway and A. Porter, *Nat. Water*, 2024, **2**, 507–508.
12 S. A. Carr, J. Liu and A. G. Tesoro, *Water Res.*, 2016, **91**, 174–182.
13 K. L. Ho, S. P. Yeap and K. M. Lee, *Environ. Pollut.*, 2025, **382**, 126658.
14 Z. Chen, J. Fang, W. Wei, H. H. Ngo, W. Guo and B. J. Ni, *J. Cleaner Prod.*, 2022, **371**, 133676.
15 M. Padervand, E. Lichtfouse, D. Robert and C. Wang, *Chem. Lett.*, 2020, **18**, 807–828.
16 L. Bai, L. Liu, M. Esquivel, B. L. Tardy, S. Huan, X. Niu, S. Liu, G. Yang, Y. Fan and O. J. Rojas, *Chem. Rev.*, 2022, **122**, 11604–11674.
17 Y. Wu, S. Chen, J. Wu, F. Liu, C. Chen, B. Ding, X. Zhou and H. Deng, *Sci. Adv.*, 2024, **10**, eadn8662.
18 X. Lin, H. Zhang, S. Li, L. Huang, R. Zhang, L. Zhang, A. Yu and B. Duan, *Carbohydr. Polym.*, 2022, **290**, 119444.
19 Y. Wu, C. Ye, F. Liu, X. Gu, L. Yu, X. Shi, Y. Du, M. Ding, C. Chen and H. Deng, *Adv. Funct. Mater.*, 2024, **34**, 2311075.
20 G. Ji, Y. Xing and T. You, *J. Environ. Chem. Eng.*, 2024, **12**, 113377.
21 G. Crini, E. Lichtfouse, L. D. Wilson and N. Morin-Crini, *Environ. Chem. Lett.*, 2019, **17**, 195–213.
22 H. B. Quesada, T. P. de Araújo, D. T. Vareschini, M. A. S. D. de Barros, R. G. Gomes and R. Bergamasco, *Int. J. Biol. Macromol.*, 2020, **164**, 2535–2549.
23 T. Krahnstöver, J. Plattner and T. Wintgens, *Water Res.*, 2016, **101**, 510–518.
24 L. Jiang, Y. Liu, S. Liu, G. Zeng, X. Hu, X. Hu, Z. Guo, X. Tan, L. Wang and Z. Wu, *Environ. Sci. Technol.*, 2017, **51**, 6352–6359.
25 S. Ling, W. Chen, Y. Fan, K. Zheng, K. Jin, H. Yu, M. J. Buehler and D. L. Kaplan, *Prog. Polym. Sci.*, 2018, **85**, 1–56.
26 J. Xu, M. Guo, M. Lin, C. Ma and G. Chen, *J. Environ. Chem. Eng.*, 2025, **13**, 115576.
27 S. Saito, Y. Matsui, Y. Yamamoto, S. Matsushita, S. Mima, N. Shirasaki and T. Matsushita, *Water Res.*, 2020, **187**, 116412.
28 Y. Zhang, J. Sun, Y. Bi, J. Gao, J. Su and S. Zhang, *Int. J. Biol. Macromol.*, 2024, **279**, 134803.
29 Y. Zhou, Y. He, X. Lin, Y. Feng and M. Liu, *ACS Appl. Mater. Interfaces*, 2022, **14**, 46980–46993.
30 C. Sun, Z. Wang, H. Zheng, S. Zhao, X. Luo, C. Li, L. Chen and F. Li, *Sep. Purif. Technol.*, 2024, **331**, 125586.
31 Y. Ji, Y. Zhuang, X. Jiao, Z. Cheng, C. Liu, X. Yu and Y. Zhang, *Small*, 2023, **19**, 2303658.
32 P. Hadi, J. Guo, J. Barford and G. McKay, *Environ. Sci. Technol.*, 2016, **50**, 5041–5049.
33 Y. Xia, H. Yuan, C. Qiao, W. Li, R. Wang, P. Chen, Y. X. Li and G. M. Bao, *J. Hazard. Mater.*, 2024, **465**, 133386.
34 Z. Li, H. Hanafy, L. Zhang, L. Sellaoui, M. Schadeck Netto, M. L. S. Oliveira, M. K. Seliem, G. Luiz Dotto, A. Bonilla-Petriciolet and Q. Li, *Chem. Eng. J.*, 2020, **388**, 124263.

35 N. F. Cardoso, E. C. Lima, B. Royer, M. V. Bach, G. L. Dotto, L. A. A. Pinto and T. Calvete, *J. Hazard. Mater.*, 2012, **241–242**, 146–153.
36 F. Liu, Y. Wu, M. Zheng, Y. Liu, S. Cao, Y. Qiu, Z. Zhao and H. Deng, *Adv. Funct. Mater.*, 2025, **35**, 2418911.
37 X. Fu, S. Zhang, X. Zhang, Y. Zhang, B. Li, K. Jin, X. Feng, J. Hong, X. Huang, H. Cao, Q. Yuan, P. Ai, H. Yu and Q. Li, *Adv. Funct. Mater.*, 2023, **33**, 2212570.
38 C. Sun, Z. Wang, L. Chen and F. Li, *Chem. Eng. J.*, 2020, **393**, 124796.
39 Z. Zhu, X. Wu, C. Wang, Z. Meng, C. Sun and Z. Wang, *Sep. Purif. Technol.*, 2023, **322**, 124321.
40 M. Ko, T. Jang, S. Yoon, J. Lee, J. H. Choi, J. W. Choi and J. A. Park, *Chemosphere*, 2024, **356**, 141956.
41 B. Zheng, B. Li, H. Wan, X. Lin and Y. Cai, *J. Hazard. Mater.*, 2022, **431**, 128611.
42 F. Liang, Y. Xu, S. Chen, Y. Zhu, Y. Huang, B. Fei and W. Guo, *ACS Appl. Mater. Interfaces*, 2022, **14**, 56027–56045.
43 J. Li, K. Wang, K. Wang, S. Liang, C. Guo, A. Hassan and J. Wang, *Colloids Surf., A*, 2024, **699**, 134671.
44 X. Fu, S. Zhang, X. Zhang, Y. Zhang, B. Li, K. Jin, X. Feng, J. Hong, X. Huang, H. Cao, Q. Yuan, P. Ai, H. Yu and Q. Li, *Adv. Funct. Mater.*, 2023, **33**, 2212570.
45 S. Huang, D. Liu, L. Zhang, Z. Zhang, S. Wang, W. Zhang, Y. Duan, L. Zong, B. Li and J. Zhang, *Adv. Mater.*, 2025, **37**, e08514.
46 L. Chen, T. Bi, E. Lizundia, A. Liu, L. Qi, Y. Ma, J. Huang, Z. Lu, L. Yu, H. Deng and C. Chen, *Innovation*, 2024, **5**, 100655.
47 M. Susana Cortizo, C. F. Berghoff and J. L. Alessandrini, *Carbohydr. Polym.*, 2008, **74**, 10–15.
48 X. Shen, T. Hussain, M. Mitchek, J. Wong and D. Reible, *Water Res.*, 2023, **236**, 119978.
49 D. X. Luong, K. V. Bets, W. A. Algozeeb, M. G. Stanford, C. Kittrell, W. Chen, R. V. Salvatierra, M. Ren, E. A. McHugh, P. A. Advincula, Z. Wang, M. Bhatt, H. Guo, V. Mancevski and R. Shahsavari, *Nature*, 2020, **577**, 647–651.
50 K. J. Silva, K. M. Wyss, C. H. Teng, Y. Cheng, L. J. Eddy and J. M. Tour, *Small*, 2025, **21**, 2311021.
51 W. A. Algozeeb, P. E. Savas, D. X. Luong, W. Chen, C. Kittrell, M. Bhat, R. Shahsavari and J. M. Tour, *ACS Nano*, 2020, **14**, 15595–15604.

